Acta Biomaterialia 142 (2022) 388–401

Contents lists available at ScienceDirect

Acta Biomaterialia

journal homepage: www.elsevier.com/locate/actbio

Full length article

Processing optimization, mechanical properties, corrosion behavior and cytocompatibility of additively manufactured Zn-0.7Li biodegradable metals

Yu Qin[a,b], Hongtao Yang[c], Aobo Liu[a,b], Jiabao Dai[a,b], Peng Wen[a,b,*], Yufeng Zheng[d,*], Yun Tian[e], Shuang Li[f], Xiaogang Wang[c]

[a] The State Key Laboratory of Tribology, Tsinghua University, Beijing, 100084, China
[b] Department of Mechanical Engineering, Tsinghua University, Beijing, 100084, China
[c] School of Engineering Medicine, Beihang University, Beijing, 100191, China
[d] School of Materials Science and Engineering, Peking University, Beijing, 100871, China
[e] Department of Orthopaedics, Peking University Third Hospital, Beijing 100191, China
[f] Beijing Advanced Innovation Center for Big Data-Based Precision Medicine, and School of Biological Science and Medical Engineering, Beihang University, Beijing, 100191, China

ARTICLE INFO

Article history:
Received 10 November 2021
Revised 15 January 2022
Accepted 20 January 2022
Available online 24 January 2022

Keywords:
Additive manufacturing
Laser powder bed fusion
Biodegradable metal
Zn-Li alloy
Porous scaffold

ABSTRACT

Biodegradable Zn-Li alloys exhibit superior mechanical performance and favorable osteogenic capability for load-bearing bone devices. Additive manufacturing (AM) endows freedom for the fabrication of bone implants of personalized structure to satisfy patient-specific needs. In this paper, AM of Zn-Li alloys was attempted for the first-time using laser powder bed fusion (LPBF), and the fabricated samples exhibited good fusion quality and high dimensional accuracy. The processing optimization, mechanical properties, *in vitro* corrosion behavior and cytocompatibility were investigated by using Zn-0.7Li bulk and porous samples. The ultimate tensile strength and elastic modulus of bulk samples respectively reached 416.5 MPa and 83.3 GPa, and both were the highest among various additively manufactured Zn alloys reported so far. Porous samples achieved compressive strength (18.2 MPa) and elastic modulus (298.0 MPa), which were comparable to those of cancellous bone. Porous samples exhibited a higher corrosion rate and alleviated the problem of slow degradation of Zn-Li alloys. Nevertheless, osteoblastic cells showed a more spreading and healthier morphology when adhering to the porous samples compared to the bulk samples, thus a better cytocompatibility was confirmed. This work shows tremendous potential to precisely design and modulate biodegradable Zn alloys to fulfill clinical needs by using AM technology.

Statement of significance

This paper firstly studied processing optimization during laser powder bed fusion of Zn-Li alloy. Bulk and porous Zn-0.7Li samples in customized design were obtained with high formation quality. The tensile strength of bulk samples reached 416.5 MPa, while the compressive strength and modulus of porous samples reduced to 18.2 MPa and 298.0 MPa, comparable to those of bone. The weight loss of porous samples was roughly 5 times that of bulk samples; osteoblastic cells showed a more spreading and healthier morphology at porous samples, indicating improved biodegradation rate and cytocompatibility. This work shows tremendous potential to precisely design and modulate biodegradable Zn alloy porous scaffolds to fulfill clinical needs by using additive manufacturing technology.

1. Introduction

As a revolutionary bioactive material, biodegradable metals (BMs) have attracted increasing attention in the research and development of bone implants [1–3]. BMs are expected to dissolve completely during implantation upon fulfilling the mission to as-

* Corresponding authors.
E-mail addresses: wenpeng@tsinghua.edu.cn (P. Wen), yfzheng@pku.edu.cn (Y. Zheng).

https://doi.org/10.1016/j.actbio.2022.01.049
1742-7061/

sist with tissue healing [4]. Compared with traditional bio-inert medical metals, BMs can achieve a full recovery of damaged bones and avoid the risk of secondary surgery [5]. Magnesium-based BMs have been widely investigated and have achieved some clinical applications, yet there are some critical technical limitations such as the fast degradation rate, the formation of hydrogen gas and the lack of mechanical strength [6]. Zinc is an essential element for bone metabolism and has a moderate corrosion rate as well as good biocompatibility in human bodies, thus has become attractive for biodegradable applications. However, pure Zn has a tensile strength of only about 45–120 MPa, which is far from sufficient. With the addition of biocompatible alloying elements, various biodegradable Zn alloys have been developed with better mechanical and biological properties [7–19].

Among various biodegradable Zn alloys, Zn-Li alloys have been recently reported with superior performances [11–19]. Zhao et al. [11] studied hot rolled Zn-xLi (x = 0.2, 0.4 and 0.7 wt.%) alloys and found Zn-0.7Li had the highest tensile strength of 569 MPa, an elastic modulus of 100 GPa, and an elongation to failure of 2.5%. Yang et al. [19] compared mechanical properties, degradation rate, cytotoxicity, and osteogenesis of binary and ternary Zn alloys with the addition of 8 different alloying elements, including Mg, Ca, Sr, Li, Mn, Fe, Cu, Ag. The addition of Li was found to be the most effective to enhance mechanical strength as well as to improve cytocompatibility and cell proliferation. Lacroix et al. [20] pointed out that Li improved bone mass in mice and enhanced bone formation via the activation of the canonical Wnt pathway. Despite the promising results, Zn-Li alloys still have several major concerns for biodegradable applications. Firstly, Zn-Li alloys possess a higher elastic modulus than bone, which leads to a stress shielding effect at the early stage of implantation [19]. Secondly, the biodegradation rate of Zn-Li alloys is too slow compared with the required term of bone reconstruction. Li et al. [12] found that the in-vitro corrosion rate of pure Zn was 45.76 μm/year, while that of Zn-1.4Li alloy decreased to 14.26 μm/year. The *in vivo* corrosion rate of Zn-0.4Li was 0.16 μm/year according to the 8 weeks' implantation results. The volume losses of Zn-0.4Li alloys were less than 10%. And it took at least 20 months for the complete degradation based on a linear degradation trend [16,19]. The last but not least, the concentration of corrosion products should be controlled within a beneficial range considering the cytotoxicity of dissolved Zn ions [7–9]. For now, though, all the reported data of Zn-Li alloys have been based on bulk materials produced by conventional manufacturing processes such as casting, rolling and extrusion.

Compared with alloying design, structural design exhibits more flexibility and efficiency to tailoring material properties. Benefiting from the development of additive manufacturing (AM), porous scaffolds of customized structure become feasible to be fabricated reliably, accurately, and efficiently [21–24]. For example, it was found that metal porous scaffolds based on triply periodic minimal surface (TPMS) provided a unique combination of properties suitable for bone implants [25–27]. Recently, laser powder bed fusion (LPBF) has been applied to Zn-based metal for the fabrication of porous scaffolds [28–39]. Wen et al. [29,30] investigated the effect of LPBF processing conditions on the formation quality and mechanical properties of Zn-based metals and achieved a reliable process. The tensile strength and elastic modulus of pure Zn reached 134 MPa and 80 GPa, equivalent to its wrought counterparts. While the compressive strength and elastic modulus of pure Zn porous samples were reduced to 23 MPa and 0.95 GPa [31,32]. Li et al. [33,34] investigated mechanical properties, *in vitro* corrosion behavior and cytotoxicity of pure Zn porous scaffolds produced by LPBF. The porous scaffolds showed an elastic modulus of 785.7 MPa and a volume loss of 7.8% after 28-day immersion tests, indicating a reduced stiffness and an accelerated corrosion rate compared with those of bulk samples. Lietaert et al. [35] studied the effect of different unit cells on the formation quality and mechanical properties. The compression strength of pure Zn porous scaffolds depended on the structure of unit cells and varied between 8 and 33 MPa with the same porosity of 70% in design.

To date, several works have been reported on the LPBF of Zn alloys [32,36–39]. Yang et al. prepared Zn-xMg alloy powders by ball mixing of pure Zn and pure Mg and produced bulk samples by LPBF. The highest relative density was 98.1%, and considerable internal defects were observed in the LPBF samples. With the addition of 3 wt.% Mg, Zn-3Mg LPBF samples showed the highest strength of 222.3 MPa. The *in vitro* corrosion rate increased with increasing the addition of Mg [36]. Qin et al. fabricated Zn-Mg bulk and porous samples by LPBF by using mixed powder of pure Zn and WE43 alloy. The relative density was over 99.5%, indicating good fusion quality. The highest strength was 335.4 MPa when 5 wt.% WE43 powder was mixed with pure Zn powder. However, the heterogeneous distribution of chemical compositions and microstructure was observed in LPBF samples due to the different densities of the two constituent powders. The fabricated structural porosity of porous scaffolds was 45%, much lower than the design value of 67% [32]. A big geometrical error existed between the designed and the fabricated porosity due to the attachment of powder particles. The deteriorated fusion quality and dimensional accuracy have been major problems for the application of Zn alloys porous scaffolds produced by LPBF, considering that Zn is highly susceptible to vaporization [40].

The powder preparation and additive manufacturing of Zn-Li alloys are regarded difficult considering the high reactivity and the low density of Li. This paper is the first attempt to introduce Zn-Li alloy structures fabricated by additive manufacturing. The Zn-0.7Li powder is prepared by pre-alloy casting followed by argon atomization. Bulk cuboids and porous scaffolds of TPMS-gyroid units are built by LPBF. Processing conditions are investigated for the optimization of fusion quality and dimensional accuracy. Microstructure, mechanical properties, corrosion behavior and cytocompatibility are characterized. The effect of porous structure on biodegradable applications of Zn-0.7Li alloy as bone implants was analyzed.

2. Materials and methods

2.1. Additive manufacturing

Zn-0.8Li (wt.%) cylinder bars in size of $\varphi 30 \times 350$ mm^3 were cast in vacuum (Hunan Institute of Rare Earth Metal Materials, China). The pre-alloyed cylinder bars were atomized into powder particles by argon gas (Nanoval, Germany). Powder particles and the as-built LPBF samples were dissolved in 5% vol.% hydrochloric acid to measure their chemical compositions by inductively coupled plasma optical emission spectroscopy (ICP-OES, iCAP6300). The content of the Li element in the powder was 0.69 ± 0.01 wt.%, so the powder was denoted as Zn-0.7Li. The powder was spherical, and the mean powder size d_{50} was 29.7 μm at the range +15/−63 μm as shown in Fig. 1(a). Compared with the Zn alloy powders prepared by ball milling [36–39] or vibration mixing [32], the atomized Zn-0.7Li powder had good flowability and uniform size distribution, critical to maintaining a stable formation quality and homogeneous microstructure during the LPBF process.

A compact LPBF machine (BLT S210, China) was used to additively manufacture bulk and porous Zn-0.7Li samples as shown in Fig. 1(b-c). The optical system consisted of a single-mode ytterbium fiber laser (IPG YLR-500, Germany) with a laser spot diameter of 70 μm at the wavelength of 1070 nm. The processing chamber was filled with argon at atmospheric pressure. The oxygen content was monitored by an oxygen meter and was kept below 100 ppm during the LPBF. The key parameters, including laser

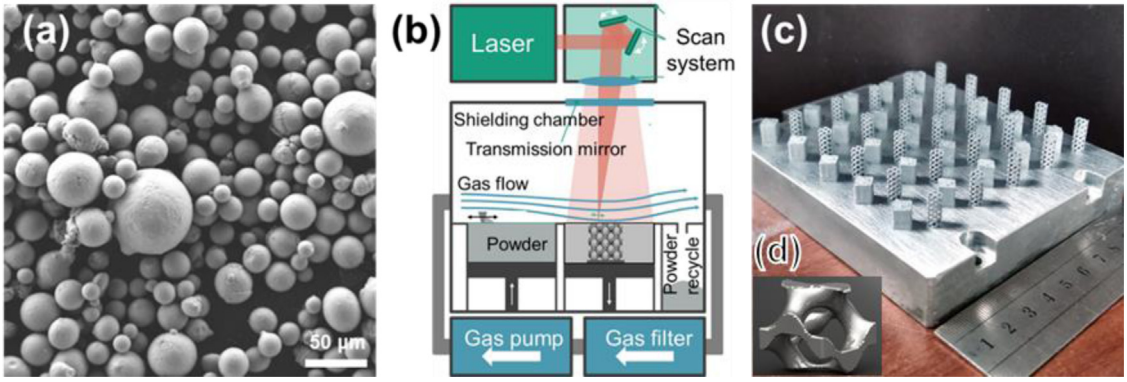

Fig. 1. (a) SEM image of pre-alloyed Zn-0.7Li powder; (b) illustration of LPBF process; (c) pictures of as-built Zn-0.7Li samples; (d) gyroid unit in design.

power P_L and scanning speed V_S, were variables to study the processing conditions. The hatch spacing H_S and layer thickness D_S were fixed as 70 and 20 μm respectively. A zig-zag exposure pattern with a 67° rotation per layer was used for bulk samples. The internal zig-zag hatching plus outline contouring exposure pattern was used for porous scaffolds [29,30]. Pure Zn metal plates with 25 mm thickness were used as the substrates. Triply periodic minimal surface (TPMS) was used to design the used porous scaffolds with uniformly distributed gyroid units according to Eq. (1) [27]. The side length of each gyroid unit was fixed as 2 mm, and the structural porosity in design was approximately 80% with the pore size of 827 μm.

$$F_{gyroid} = sin(\pi x)cos(\pi y) + sin(\pi y)cos(\pi z) + sin(\pi z)cos(\pi x) - 0.9 \quad (1)$$

After the LPBF process, the fusion quality and dimension accuracy were characterized by using the relative density of bulk samples and the fabricated structural porosity of porous samples. The bulk samples in size of 6 × 6 × 6 mm^3 were cut, grinded and polished. The cross-sections were parallel to the building direction. Five different regions were picked up randomly from the cross-sections of bulk samples. The total area of void defects (A_{void}) was measured for each region (A_{total}) by imaging binarization and was used to calculate the relative density (ρ_s) according to Eq. (2) [29,30]. The designed and fabricated structural porosity (*DP* and *FP*) of porous samples in size of φ5 × 6 mm^3 were calculated by Eq. (3) and Eq. (4) respectively. The surface area (A_d) and volume (V_d) of porous samples in design were obtained by using the numerical model. The fabricated volume of porous samples (V_f) was calculated by Eq. (5) according to the Archimedes method. M_a and M_e are the mass of samples measured in air and ethanol respectively; while ρ_e is the density of ethanol. V_{ds} indicates the volume of a solid cylinder with the same outline size as that of the used porous sample [27]. The structural porosity refers to the structural geometry of porous scaffolds, related to porous design and dimensional accuracy, while the processed porosity (1-ρ_s) indicates void defects at the cross-sections of LPBF samples, related to fusion quality.

$$\rho_s = (1 - A_{void}/A_{total}) \cdot 100\% \quad (2)$$

$$DP = V_d/V_{ds} \cdot 100\% \quad (3)$$

$$FP = V_f/V_{ds} \cdot 100\% \quad (4)$$

$$V_f = (M_a - M_e)/\rho_e \quad (5)$$

2.2. Microstructure and mechanical test

The microstructure of the as-built Zn-0.7Li samples was characterized using a scanning electron microscope (SEM, Zeiss, Germany) after polishing and etching with 2 vol% hydrogen nitrate for 10 s. Phase identification was conducted by X-ray diffraction (XRD, Rigku D/max-2550, Japan) with CuKα radiation at 40 kV and 150 mA, using a continuous scan mode. A quick scan at 4°/min was conducted over a range of 2θ = 10–90° to give a general overview of the diffraction peaks. Specimens for transmission electron microscopy (TEM, FEI Tecnai F20, Netherland) observation were mechanically thinned to 80 μm and then reduced by electrolytic jet polishing. All tests were conducted on cross-sections parallel to the building direction.

Mechanical tests were carried out for the as-built samples including hardness, tension and compression. Before the test, all the specimens were ultrasonically cleaned in ethanol. Vickers hardness was measured with a load of 300 g. Ten measurements were made at the center cross-section of bulk samples that were parallel to the building direction. Tensile tests with bulk samples (10 × 10 × 2 mm^3) and compression tests with porous samples (φ5 × 6 mm^3) were conducted using a universal testing machine (Shimadzu AG-X100KN, Japan) at room temperature (~20 °C) according to ASTM 8E and ASTM E9–2009 standards. The strain rate was set as 0.05 /min, and the deformation velocity was 0.15 mm/min and 0.3 mm/min for tensile and compression tests considering the test length of samples, respectively. After the tensile test, the fresh fracture surfaces were observed using SEM. The area of the outer circular profile in a diameter of 5 mm was used as the cross-section to calculate the stress of the porous samples. Three replicate pieces were tested to obtain the average value and the standard deviation for the mechanical tests.

2.3. In-vitro corrosion test

Bulk cylinders and porous scaffolds, both in size of φ10 × 2 mm^3, were manufactured by LPBF. They were immersed in Hank's solution with an electrochemical workstation (Metrohm AG, Switzerland). For bulk cylinders, both as-built and polished surfaces were measured to investigate the effect of surface roughness on corrosion behavior. Surface roughness was measured by using a white-light interference microscope (ZYGO Nexview, USA). The scaffolds were fully exposed to the solution by a customized graphite fixture. A three-electrode system was used with a working electrode (Zn-0.7Li samples), a reference electrode (saturated calomel), and a counter electrode (platinum). The potential dynamic polarization (PDP) was determined at a scan rate of 1 mV/s. Corrosion potential (E_{corr}) and corrosion current density (I_{corr}) were calculated by a linear fit and Tafel extrapolation. At least five measurements were conducted for each group. Electrochemical impedance spectroscopy (EIS) was performed over a frequency range of 10^{-2}–10^5 Hz with a perturbation of 10 mV. The corroded surfaces were observed by SEM and Energy dispersive

x-ray spectroscopy (EDS) before and after the removal of corrosion products.

Immersion tests were performed on bulk and porous samples using Hank's solution (at 37 °C, pH 7.4) for 28 days according to ASTM-G31–72. The outline dimensional size was 8 × 8 × 2 mm^3 for bulk samples and φ5 × 6 mm^3 for porous samples respectively. The exposure ratio of Hank's volume to the test surface area was fixed as 20 mL/cm^2. The pH value of Hank's solution was recorded using a pH meter (Mettler FiveEasy pH FE20 K, Switzerland). After immersion, the samples were cleaned using distilled water, and the corroded surfaces were observed using SEM and EDS. The weight loss was evaluated by using an electronic balance (±0.1 mg) after the corrosion products were removed by using a CrO_3 solution. The corrosion rate (*CR*) of immersed samples was calculated by Eq. (6). *W* is the weight loss; A_d is the surface area in design; *t* is the immersion time; ρ is the standard density. After 28-day immersion, compression tests were carried out on the porous samples after removing the corrosion products by CrO_3 solution to investigate the effect of corrosion on the mechanical strength. Three replicate samples were measured for each condition.

$$CR = W/(A_d \cdot t \cdot \rho) \tag{6}$$

2.4. Biocompatibility test

MC3T3-E1 pre-osteoblasts were used to investigate the cell adhesion on the LPBF samples. Cell suspension of 50 µL, containing 18 × 10^5 cells, was carefully spread all over the surface in 24-well culture plates. Cell attachment was allowed for 2 h. All samples were transferred into a new 24-well plate, and 2 mL of fresh culture medium was added into each well subsequently. After being cultured 24 h, cells were fixed in 2.5% glutaraldehyde solutions for 1 h. The samples were dehydrated in gradient diluted alcohol (50%, 60%, 70%, 80%, 90%, 95%, 100%). and then dehydrated overnight in the 24-well plate. The cell morphology was observed by SEM. Cytoskeletal staining using DAPI and FITC phalloidine was applied to evaluate the cell morphology. After culturing for 24 h, the samples were washed three times with PBS solution and fixed with 4% paraformaldehyde solution for 20 min at room temperature. The cells were permeabilized with 0.5% Triton X-100 for 10 min. F-actin and nuclei were stained with FITC-phalloidin and DAPI. Finally, cytoskeletal(green) and nuclei (blue) of the cells on the samples were observed by laser scanning confocal microscopy (LSCM).

2.5. Statistical information

All the experiments and measurements were carried out with three replicates at least. All data were presented as means ± deviations. Tukey's method was applied for the comparison between different groups. Values of *p* less than 0.05 were considered statistically significant.

3. Results

3.1. Formation quality

Fig. 2(a) illustrates the distribution of the relative density (ρ_s) with various laser power (P_L) and scanning speed (V_S) for bulk samples. Generally, the relative density decreased with increasing P_L; while it increased at first, then decreased with increasing V_S. The highest relative density reached over 99.5% at the processing condition PC1 with $P_L = 40$ W and $V_S = 800$ mm/s. Only some spherical micropores in the size of dozens of microns were observed. Fig. 2(b-d) shows typical cross-sections under conditions around PC1. With a lower V_S at PC2, the excessive energy input (P_L/V_S) caused more vaporization, and more pore defects were observed. With a higher V_S at PC3, the insufficient energy input couldn't fully melt all the powder particles, and a lack of fusion was found. The pore defects are distributed randomly, while the lack of fusion defects is located continuously between the layers. With $P_L = 120$ W and $V_S = 600$ mm/s at PC4 in Fig. 2(e), the energy input was so large that vaporization and thermal distortion together led to collapsed samples. Further increasing the energy input failed to obtain complete samples, therefore no data was presented at the range of $P_L \geq 100$ W and $V_S \leq 400$ mm/s in Fig. 2(a). Overall, the fusion quality was considerably sensitive to the laser energy input determined by P_L and V_S regarding the LPBF of Zn-0.7Li.

Fig. 3(a) demonstrates the distribution of the fabricated structural porosity (*FP*) of porous samples with various P_L and V_S. All the *FP* decreased less than the designed structural porosity (*DP*) of 80%, owing to powder attachment resulting by extra melting and wetting of powder particles. A higher *FP* approaching 80% indicated higher dimensional accuracy. Generally, the *FP* decreased with increasing P_L or decreasing V_S. A relatively low energy input alleviated the extra melting and wetting. The highest *FP* reached 78.9% at PC3. Fig. 3(b) shows the pictures of typical porous samples. Compared with PC3, the attached powder particles at PC8 severely clogged the pores, leading to a low *FP*, namely a high dimensional error between the designed and fabricated structures. Fig. 3(c-e) shows the cross-sections of the struts of porous samples. With P_L = 40 W and V_S = 1000 mm/s at PC3, the balanced fusion quality and dimensional accuracy were achieved. Eventually, PC1 and PC3 were used for the fabrication of bulk and porous samples respectively.

3.2. Microstructure

The content of Li element in the LPBF samples was 0.68 ± 0.01 wt.% measured by ICP-OES, a bit lower than 0.69 ± 0.01 wt.% in the powder. The content of harmful elements, including Cu, Ni, Cr and Fe, were detected less than 0.01% for both the powder and the LPBF samples. The small error of Li content among different samples implies a homogeneous distribution of chemical compositions. The decreased content of the Li element in the LPBF samples implies that the relative vaporization loss of Li was bigger than that of Zn during the LPBF process. XRD patterns in Fig. 4(a) show that both Zn-0.7Li powder and LPBF samples contained α-Zn and β-$LiZn_4$ phases, which were also found in hot-rolled Zn-0.7Li alloy [11]. There are also some unidentified small peaks in the XRD patterns, which were reported in the previous literature as well and require further investigation by some advanced measurement approaches. Based on the binary Zn-Li phase diagram, β-$LiZn_4$ will further decompose into α-Zn and α-$LiZn_4$ at 65 °C [12]. However, the cooling rate during the LPBF process is too fast to drive β-$LiZn_4$ into decomposition. Accordingly, no α-$LiZn_4$ was found in the prepared LPBF samples. The uniformly distributed microstructure was achieved in the LPBF samples. Small round dot-like particles were found according to SEM observation as shown in Fig. 4(b). According to the dark-field TEM observation in Fig. 4(c), those particles were confirmed as second phases. Fine grains and smaller subgrains were also found. During the LPBF process, the moving laser spot resulted to a rapid cooling rate, uneven temperature distribution and thermal stress. Since Zn has a high thermal expansion coefficient and a low recrystallization temperature, the recrystallization of Zn-Li alloys was expected [13]. It should be noticed that the Li atom is difficult to be detected by the EDS analysis due to its small atomic mass. Both of α-Zn and β-$LiZn_4$ have hexagonal close-packed (HCP) lattice structures. The α-Zn has lattice parameters as a = 0.2665 nm, c = 0.4949 nm, and the c/a ratio as 1.86, while a = 0.278 nm, c = 0.439 nm, and the c/a ratio as 1.58 for β-$LiZn_4$ [15]. As indicated by the selected area electron diffraction (SAED) in Fig. 4(d), the α-Zn phases orient along $[2\bar{1}\bar{1}0]$ zone axis

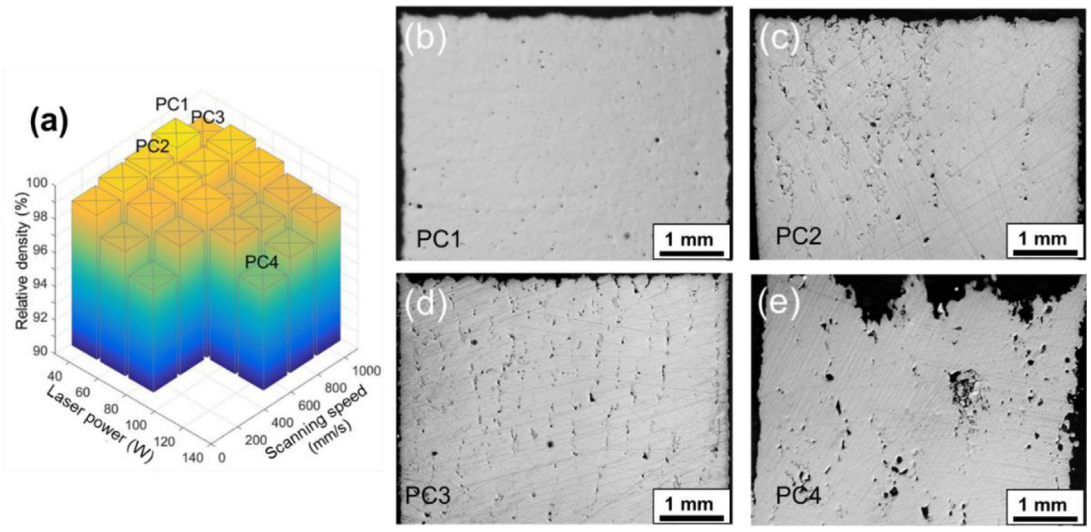

Fig. 2. Formation quality of bulk samples: (a) relative density under different processing conditions (PC); (b)-(e) typical pictures of cross-sections.

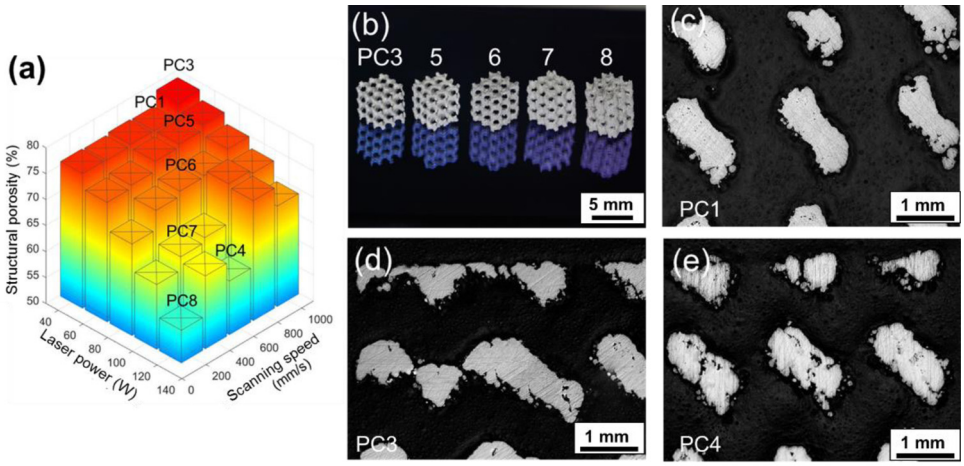

Fig. 3. Formation quality of porous samples: (a) fabricated structural porosity under different processing conditions (PC); typical pictures of the scaffolds (b) and the cross-sections of the struts (c)-(e).

with c/a as 1.9, while they along [1$\bar{2}$13] zone axis with c/a as 1.6 for the β-$LiZn_4$ phase.

3.3. Mechanical properties

The hardness was 113.4 ± 8.6 HV at the center of Zn-0.7Li LPBF samples, much higher than that of pure Zn counterparts approximately 40 HV [31]. Fig. 5(a) shows the schematics and dimensional sizes of specimens for tensile and compressive tests. The yield strength, ultimate tensile strength and Young's modulus of bulk samples were 359.1 ± 1.7 MPa, 416.5 ± 13.2 MPa and 83.3 ± 4.9 GPa respectively as shown in Fig. 5(b). The compressive strength and elastic modulus of porous samples were 18.2 ± 0.7 MPa and 298.0 ± 54.2 MPa respectively as shown in Fig. 5(c). The compressive elastic modulus of porous samples was roughly 0.4% of the tensile one of bulk samples. Fig. 5(d) illustrates the average stress-strain tensile curve of bulk samples, and the elongation at fracture was approximately 2.3%, indicating limited ductility. After the elastic region, the stress decreased a bit with increasing the strain. Fig. 5(e) exhibits the average stress-strain compressive curve of porous samples. The stress increased sharply at first to its peak value around 18.2 MPa, then declined and fluctuated. The elastic stage had a compression rate of about 6.0%. Unlike the brittle fracture along 45° frequently observed in brittle structures, the Zn-0.7Li porous samples were crushed layer-upon-layer indicated by the oscillation in the stress-strain curve, implying that the deformation capacity can be improved by a suitable porous design.

As shown in Fig. 6(a), the tensile fracture surfaces were rough with undulating ridges and valleys. No macroscopic defect was observed at the surface, while multiple cracking originated in a different direction. Few dimples were found, complying with the low elongation and brittle fracture. As shown in regions 1 and 2 in Fig. 6 (b-c), micropores and cracks were detected. The pore size was less than 20 μm. The internal surface of the pores was smooth, indicating gas pores. A typical river-like cleavage fracture was found on both sides of the crack. The microstructure at the fracture surface was very fine and homogenous. No grain boundaries or inclusions were observed, implying transgranular rupture.

3.4. Corrosion by electrochemical test

Electrochemical properties were measured to investigate the corrosion behavior of Zn-0.7Li samples. The bulk samples were further divided into two groups with as-built and polished surfaces; while as-built surfaces were tested for all the porous sam-

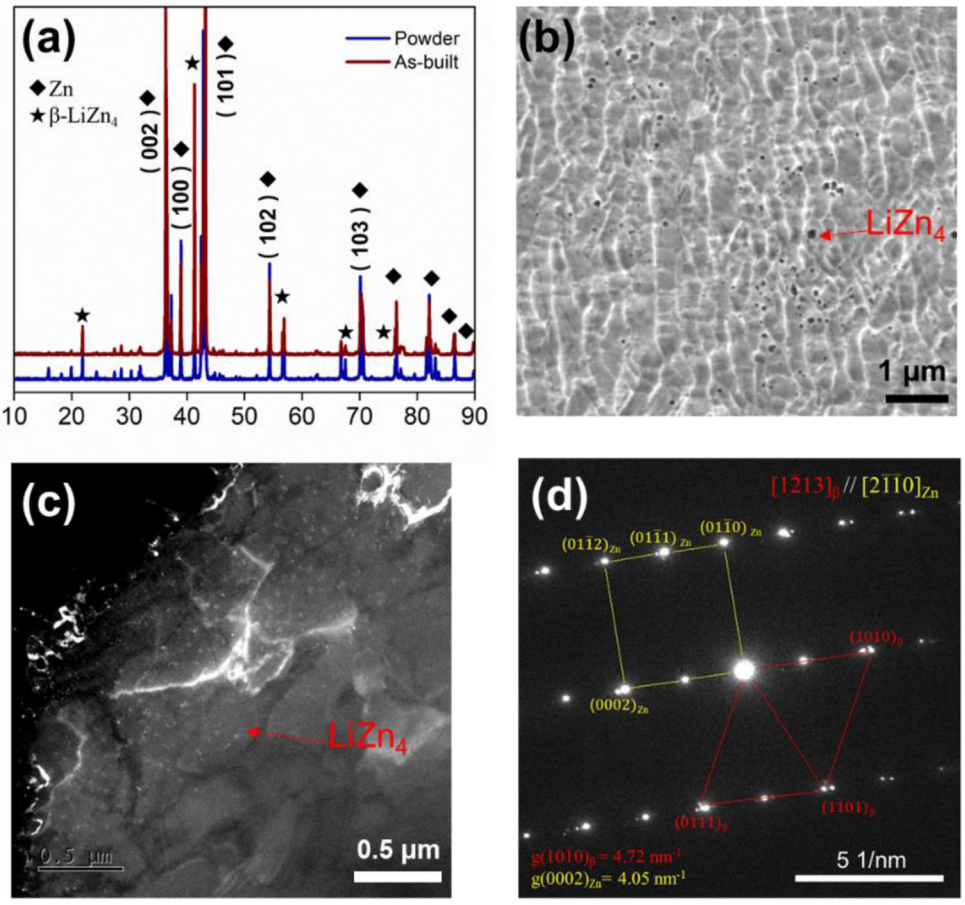

Fig. 4. (a) XRD pattern of powder and LPBF samples; (b) SEM picture; (c) dark-field TEM image with bright β-$LiZn_4$ precipitates; (d) SAED patterns along $[1213]_{\beta}$ // $[2110]_{Zn}$ axis.

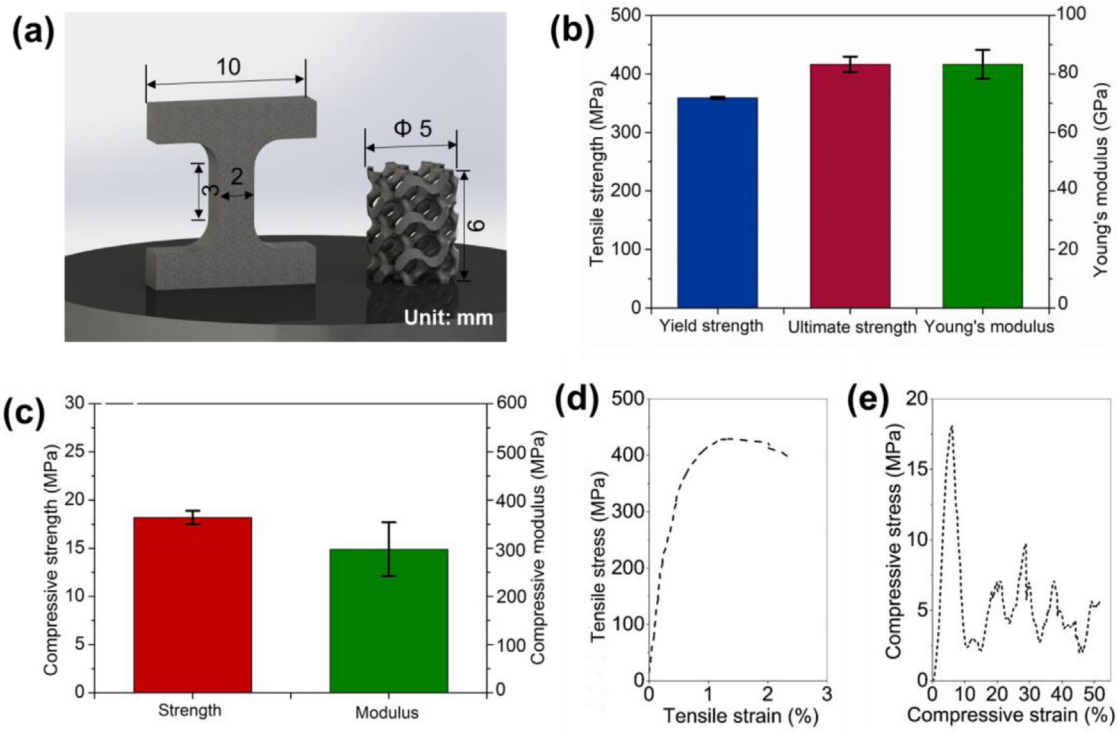

Fig. 5. Mechanical properties: (a) schematic of tensile and compression samples; (b) and (d) tensile properties and stress-strain curve of bulk samples; (c) and (e) compressive properties and stress-strain curve of porous samples.

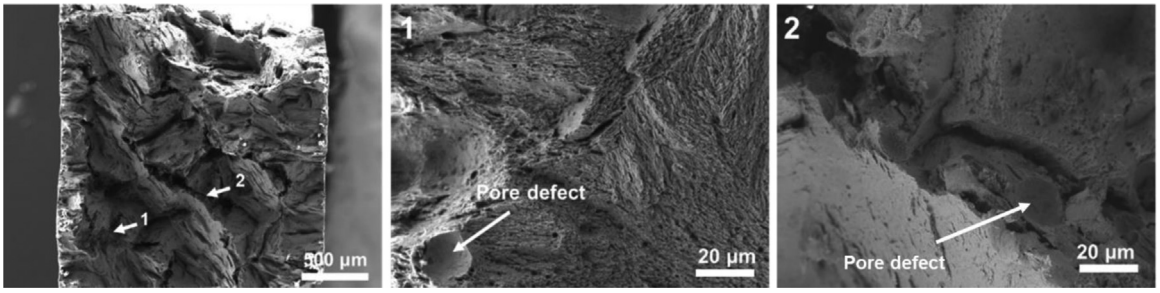

Fig. 6. Macroscopic tensile fracture surface with enlarged pictures of region 1 and region 2.

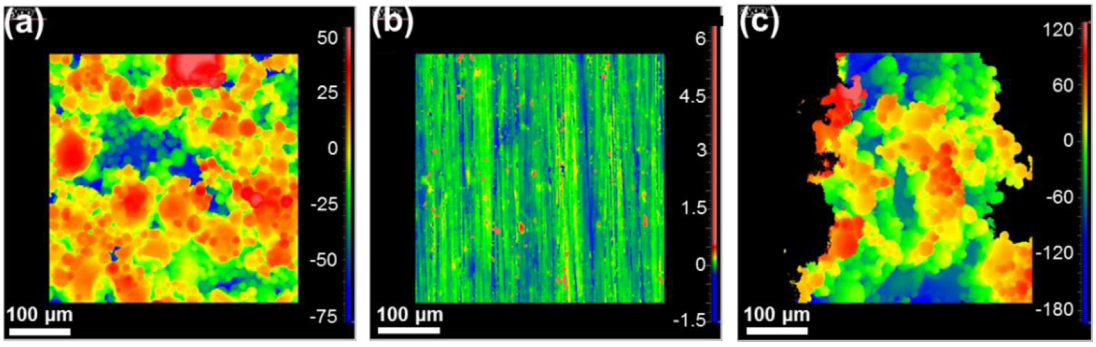

Fig. 7. Surface morphology and roughness: (a) as-built and (b) polished bulk samples and (c) strut of the porous sample.

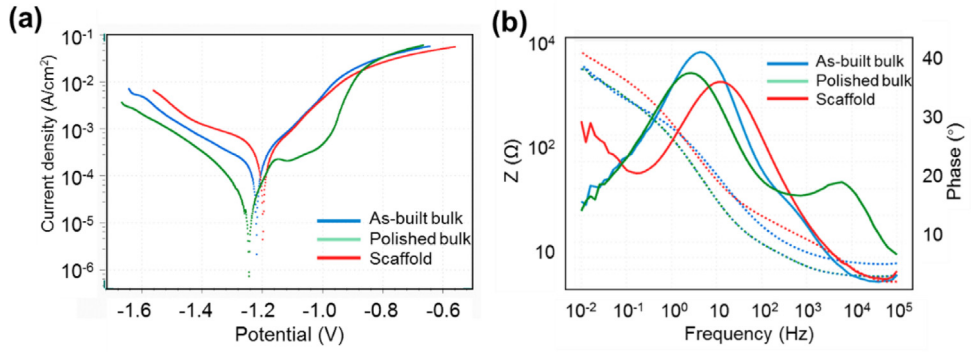

Fig. 8. Electrochemical behavior: (a) PDP curves, (b) Bode plots.

ples. As shown in Fig. 7, the surface roughness *Sa* was 0.07 ± 0.01, 17.3 ± 0.4 and 36.7 ± 1.3 μm respectively for as-built, polished bulk samples, and struts of porous samples. The increased roughness at the as-built surface was attributed to the attached powder particles, and the surface roughness of porous samples was higher than that of bulk samples. As shown in Fig. 8(a), PDP curves indicate a tremendous difference in corrosion behavior among the three types of LPBF samples. A significant stable passivation zone was observed ranging from −1.1 V to −0.9 V in anodic branches at polished bulk samples, which was indicated by the slow increment of current density and presumably caused by the formation of Li-rich passive layers [11,12,17,18]. However, compared with polished samples, no distinct passivation was found in the PDP curves of as-built bulk and porous samples.

The corresponding measurement data from Fig. 8(a) are listed in Table 1. The design data was used for the surface area without regarding the fabrication roughness. The specific area was calculated by the test area divided by the test volume of samples. It can be seen that the specific area of porous samples was roughly 9 times that of bulk samples. The corrosion potential (E_{corr}) of porous samples was slightly higher than those of bulk samples. After dividing the surface area, the current density (I_{corr}) of porous and as-built bulk samples were similar and were approximately 5 times that of polished bulk samples. Fig. 8(b) shows the Bode plots from the EIS spectra. The peak impedance of porous samples in the low-frequency (0.01–1 Hz) phase implies that there might be an inherent passivation effect at the surface of porous samples before the electrochemical tests. The larger specific surface area of porous

Table 1
Electrochemical parameters of Zn-0.7Li samples.

Sample types		Test area in design (cm^2)	A specific area in design (cm^{-1})	E_{corr} (V_{SCE})	I_{corr} (μA/cm^2)
Bulk sample	Polished	1.7	11.0	−1.26±0.03	28.5 ± 1.6
	As-built	1.7	11.0	−1.22±0.01	101.0 ± 4.1
Porous sample		2.3	96.3	−1.20±0.02	111.2 ± 12.2

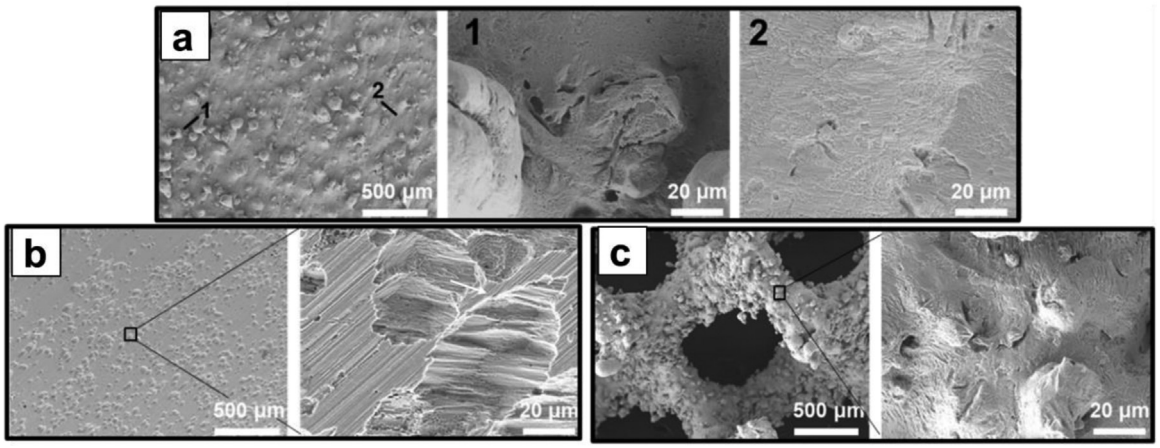

Fig. 9. Morphology of electrochemical test after the removal of corrosion products (a) as-built and (b) polished surface of bulk samples, (c) porous samples.

samples made them susceptible to oxidation at room temperature. Such corrosion layer was not obvious on the surface of bulk samples, therefore no phase peak in the low-frequency region was found. In the mid-frequency region (1–10 Hz), both porous and bulk samples show similar peaks, meaning the generation of corrosion products. The released ions diffuse more slowly inside the porous samples, and a frequency gap is found between porous and bulk samples. In the high-frequency region, polished bulk samples show a phase peak, indicating the passivation effect; on the contrary, no high-frequency peaks can be found for the as-built bulk and porous samples, implying the lack of passivation.

The corroded surfaces were further observed by SEM and EDS as shown in Fig. 9. After the removal of corrosion products, rough surfaces with attached powder particles was observed for as-built bulk samples. Bumpy locations with attached powders (point 1) corrode preferentially, and no obvious pits are observed; while shallow laminar structures uniformly distribute at other flat areas (point 2). For the polished bulk samples as shown in Fig. 9(b), typical corrosion pits with internal laminar structures distribute uniformly at the surface. The corroded surface of porous samples in Fig. 9(c) is covered with more powder particles and shows a similar morphology compared with the as-built bulk samples. The morphology of corrosion products is shown in Fig. 10. A continuous layer of corrosion products enriched in oxygen is observed at the surface of polished bulk samples. The distribution of the Li element can't be detected by EDS mapping owing to the small atomic mass. In contrast, such a continuous layer can't be found, and more corrosion products are observed at the as-built surface of bulk and porous samples. The attached powder particles corrode at first, indicated by the enrichment of O, while the surrounding substrate shows less corrosion. In summary, the electrochemical behavior of a polished surface is quite different from that of an as-built surface. The as-built surface of LPBF samples can't form dense corrosion products and doesn't show the passivation effect, which is observed at the polished surface of LPBF samples. A similar passivation effect has been reported in conventionally manufactured Zn-Li samples [11,12,17,18].

3.5. Corrosion by immersion test

The effect of porous structure on corrosion behavior was further investigated by the immersion test using as-built bulk and porous samples. Fig. 11(a) shows the changes in pH values during the 28-day immersion in Hank's solution. The pH values increased sharply on the first day, after which they showed small fluctuations and finally became stable. Corresponding to the pH values, the weight loss underwent a rapid increase in the early stage, followed by a nearly linear slow rise with increasing immersion time as shown in Fig. 11(b). Both figures imply that the Zn-0.7Li samples had a rapid corrosion rate at the initial stage, and the corrosion tended to slow down as the corrosion products accumulated over time. After 28-day immersion, the weight loss of bulk samples was 0.56%, much less than 2.60% of porous samples. The corrosion rates of bulk and porous samples calculated from the volume loss and surface area were 46.2 ± 8.1 μm/year and 35.3 ± 7.2 μm/year. Despite that a bigger structural damage was observed for the porous samples, the commonly used corrosion rate as shown in Eq. (6) failed to reflect the fact. Fig. 11(c) shows the effect of 28-day immersion on the compressive properties of porous samples. The compressive strength decreased from 18.2 to 12.9 MPa, while the elastic modulus decreased from 298.0 to 100.1 MPa.

Fig. 12(a) shows the morphology of top surfaces of porous samples before and after 28-day immersion. Flocculent corrosion products were observed at the surface of struts. The diameter of the strut decreased from 404 μm to 372 μm. The reduced diameter led to a sharp decrease in strength. Fig. 12(b) shows the morphology of as-built bulk samples. A large number of powder particles was observed at the surface before the immersion. After 7-day immersion, the number of attached powder particles was considerably reduced. After 14-day immersion, the flocculent corrosion products substantially increased, and the attached powder particles were barely visible. As the immersion time further increased, more corrosion products accumulated, and there was a large number of petal-like corrosion products after 28-day immersion. The cross-sections after 28-day immersion were examined to analyze the formation of corrosion products. As Fig. 12(c) shows, enriched elements containing C, O and Ca were found in the corrosion product.

3.6. Cytocompatibility

The MC3T3-E1 cells were used to evaluate the cell adhesion at the surface of Zn-0.7Li samples. Fig. 13 illustrated distinct cell behaviors between bulk and porous samples. The cells were shrunk in a spherical shape, and separated at the surface of as-built bulk samples, implying a relatively poor cytocompatibility by comparing with the negative Ti control group. While the cells spread out and connected by the stretched pseudopods, indicating a healthier cell morphology at the surface of porous samples. Fig. 14 presents fluorescent morphologies of cell attachment on the samples. Supplementary videos demonstrate fluorescent 3D images. The undulation of attached cells reflected the roughness of the side surface of the bulk samples. Uniform distribution of cells in the z-axis direction of the porous samples demonstrated the inward growth of

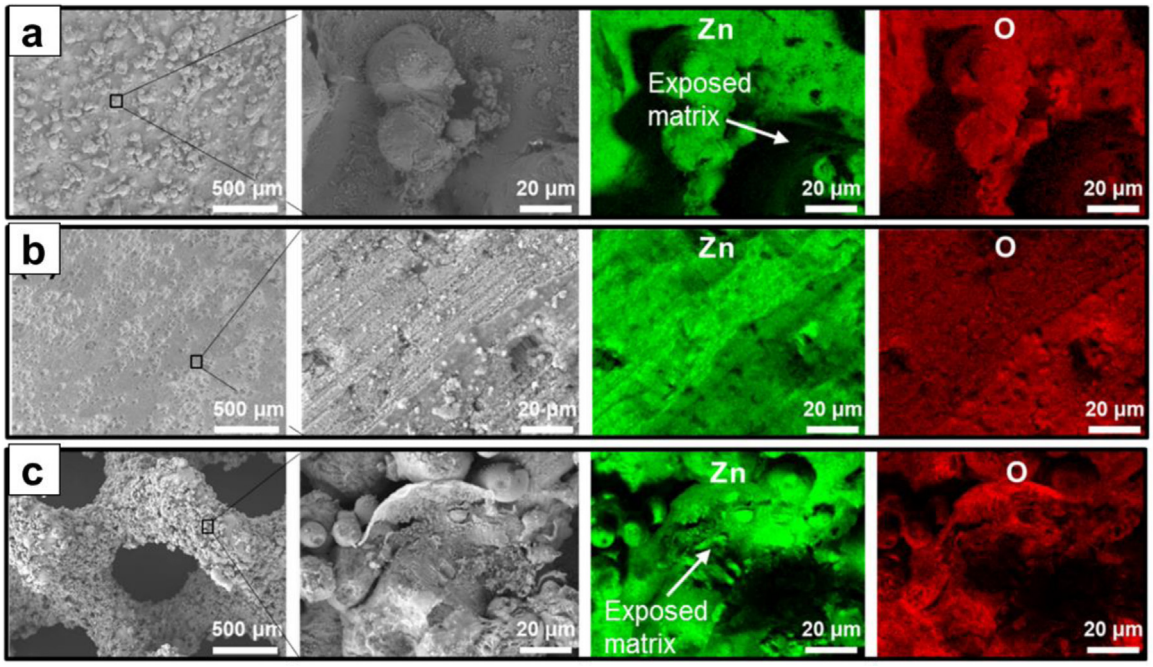

Fig. 10. Morphology and chemical composition of electrochemical test before the removal of corrosion products (a) as-built and (b) polished surface of bulk samples, (c) porous samples.

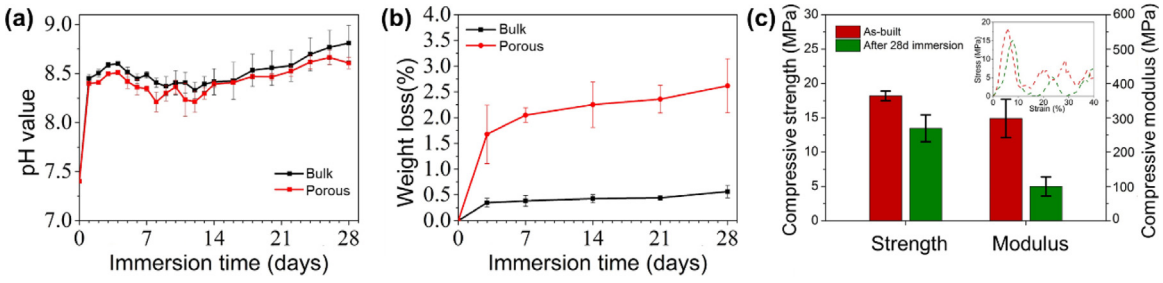

Fig. 11. Corrosion behavior by immersion test: (a) pH values, (b) weight loss, (c) Compressive strength and modulus before and after 28-day immersion.

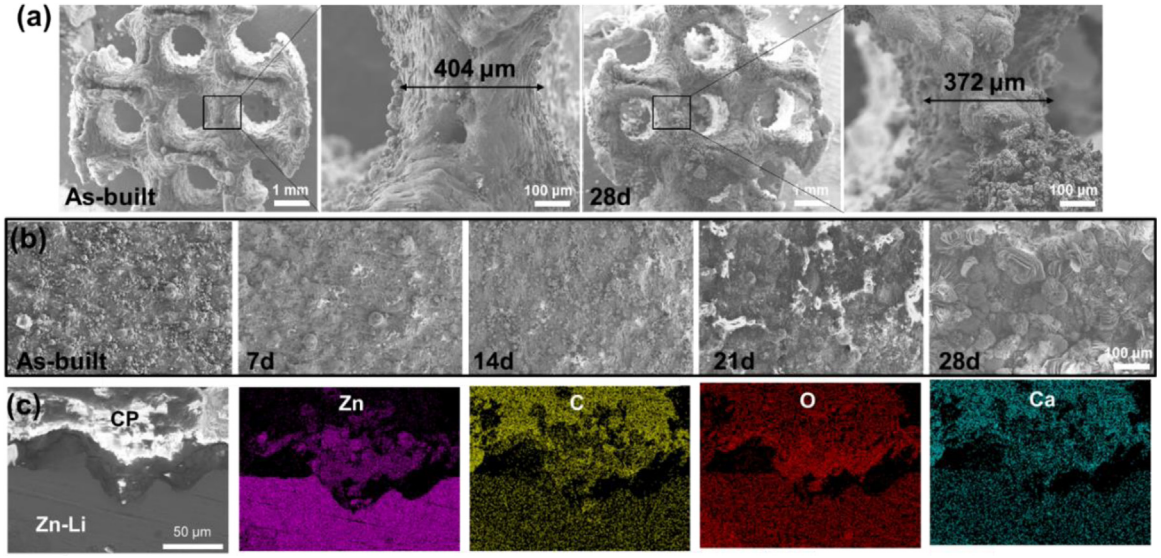

Fig. 12. Morphology before and after immersion test: (a) porous samples; (b) as-built bulk samples; (c) SEM image and elemental mapping at the cross-section of corrosion products after 28-day immersion test.

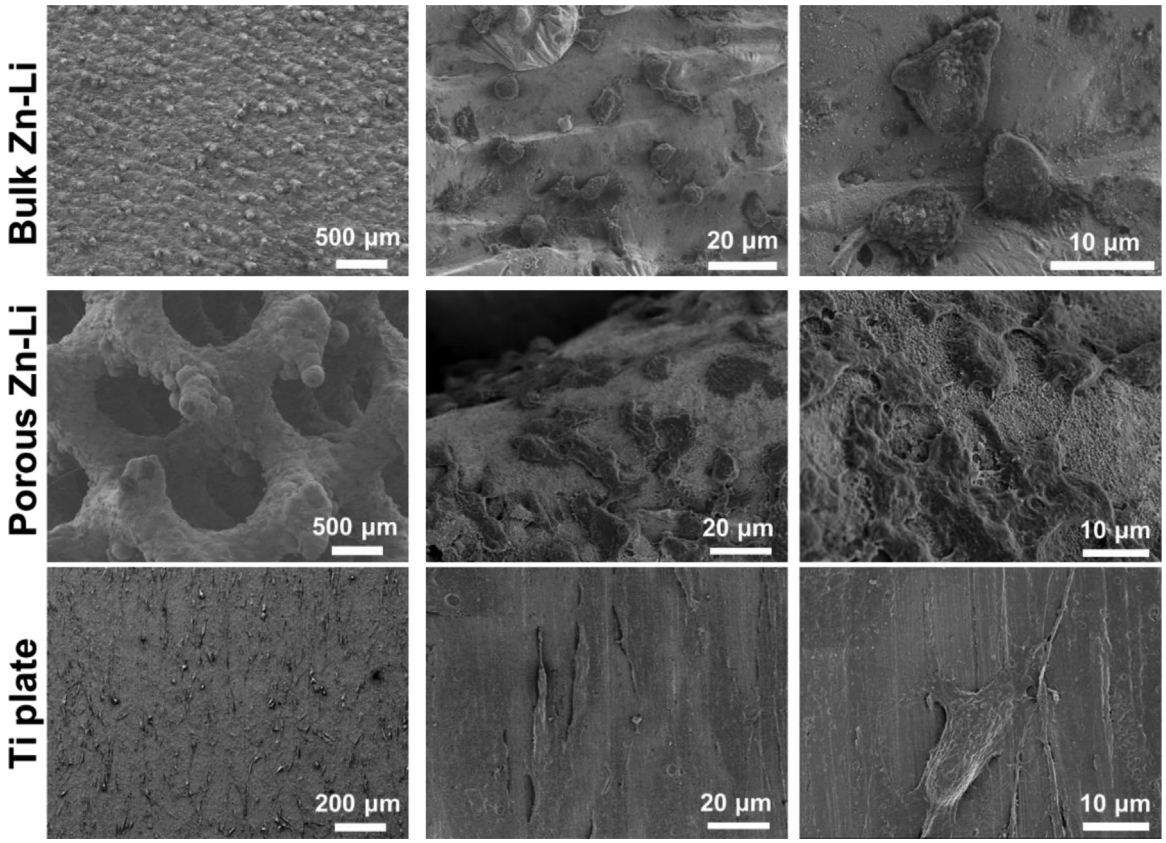

Fig. 13. Cell morphology at the surface of as-built bulk and porous samples, Ti plates were used as the negative control group.

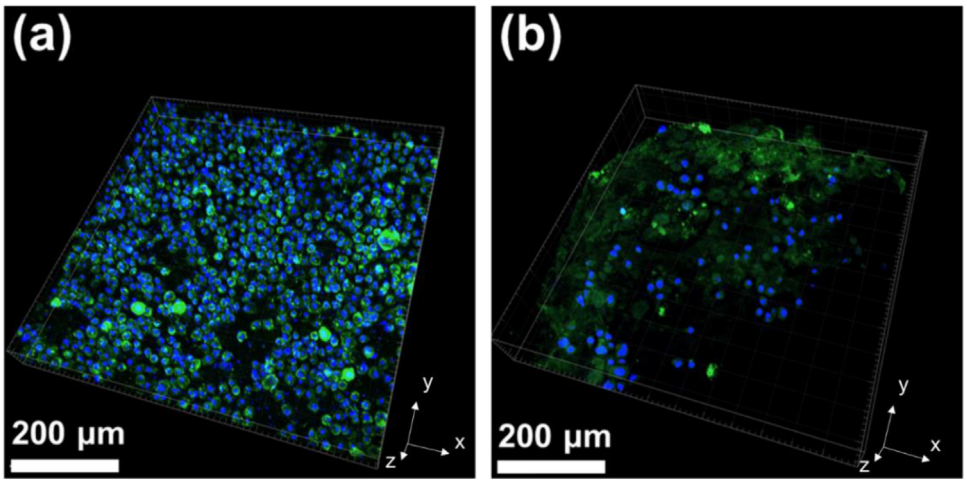

Fig. 14. Fluorescent images of cell attachment on (a) as-built bulk samples and (b) porous samples after 12 h culturing, Cell nucleus: DAPI, F-actin: FITC.

cells. Corresponding to the SEM results, the cells on bulk samples were spherical, while the cells on porous samples owned spreading actin, which further confirmed the better biocompatibility of porous samples.

4. Discussion

4.1. Processing optimization

LPBF process uses a focused laser beam of high energy intensity to selectively melt thin layers of metal powder. The process takes numerous hours until the required 3D part is additively built [22]. The performance of LPBF parts is sensitive to the processing condition and is influenced by the characteristics of powder particles, such as powder morphology, size, densification and composition. Gas atomization (GA) and plasma rotating electrode process (PREP) are common approaches to prepare the LPBF powder [41]. Supplementary Table S1 collects thermophysical properties of pure Zn, Li, Mg and Fe for reference [31,42,43]. It is challenging for the preparation of Zn-Li alloy powder owing to the high vaporization and reactivity of relevant components. Mechanical alloying methods such as ball milling and vibration mixing were used to prepare biodegradable Zn alloy powder such as Zn-Mg, Zn-Al, Zn-Ag, Zn-Graphene, etc. [36–39]. However, the alloyed powder by ball milling showed irregular morphology and size, which deteriorated powder flowability and caused unstable fusion quality. The alloyed

powder by vibration mixing resulted in an uneven distribution of components due to their different density, which in turn led to a heterogeneous distribution of composition and microstructure in the LPBF parts [32]. By using pre-alloy casting and argon atomization, high-quality Zn-0.7Li alloy powder particles were obtained in this work as shown in Fig. 1.

Regarding laser welding of Al-Li alloys, the addition of Li narrowed down the processing window and increased formation defects such as undercut and porosity [44]. Liu et al. investigated the effect of Li on powder preparation and the LPBF of Al-Li alloys. They cast Al-Li ingots at first, atomized them into Al-14Li (at.%) powder, and finally obtained Al-12.7Li (at.%) bulk samples by LPBF. The highest relative density was only 80%, indicating poor fusion quality [45]. This work was the first report on the LPBF of Zn-Li alloys and the relative density reached 99.5%. Compared with pure Zn [29], the processing window was much narrower, and the optimal energy input was much lower for the LPBF of Zn-0.7Li as shown in Fig. 2(a). The Li content reduced from 0.690 in powder to 0.675 (wt.%) in LPBF samples. According to Zhao et al. [46], the vaporization flux of a specific element in alloys is positively related to its equilibrium vapor pressure and negatively to its molecular weight. Although the equilibrium vapor pressure of Li is slightly lower than that of Zn, the molecular weight of Li is much lower than that of Zn, which explains the compositional change between the starting powder and the fabricated Zn-0.7Li sample.

Compared with bulk samples, the processing window of porous scaffolds to achieve high relative density was bigger as shown in Fig. 2 and Fig. 3. The P_L/V_S combined the influence of laser power and scanning speed together, and the increased energy input resulted in a larger molten pool, a higher temperature, and a slower cooling rate. With the energy input at PC5, it was unable to obtain a complete bulk sample, but feasible for building a porous scaffold. Porous scaffolds consisted of circular solid struts in diameter of 400 μm, thus less heat accumulation and thermal stress were caused on the small sectional area during the LPBF process. However, the increased laser energy input led to a thicker strut and a lower fabricated porosity than the designed values. With the optimized energy input at PC3, the dimensional error was as low as 1.12% regarding the discrepancy between the designed and fabricated porosity of porous scaffolds, much lower than 7% reported for pure Zn [33] and 22% reported for Zn-WE43 porous scaffolds [32]. The fusion defects inside the struts deteriorate mechanical properties, and the strength of porous scaffolds is exponentially related to the fabricated porosity, therefore the processing optimization is critical to achieving porous scaffolds of stable mechanical performance.

4.2. Mechanical properties

Biomechanics, biodegradability, and biocompatibility are necessary criteria to evaluate the performance of materials and structures of biodegradable implants. Tensile properties of bulk samples can characterize the influence of processing conditions, formation quality, and microstructure during additive manufacturing processes, and are used to make a comparison with those in conventional manufacturing such as casting, rolling and extrusion. The ultimate tensile strength of Zn-0.7Li samples reached 416.5 MPa and was the highest value reported for biodegradable Zn alloys fabricated by LPBF, approximately 3 times that of pure Zn [30], 2 times that of Zn-3Mg [36] and 1.25 times that of Zn-5WE43 [32].

The tensile strength of Zn-0.7Li LPBF samples has achieved highest among LPBF of Zn alloys. However, compared with the ultimate tensile strength and elongation of hot-rolled Zn-0.7Li (560 MPa, 2.5%) [11] and extruded Zn-0.4Li (520 MPa, 5.0%) [19], LPBF Zn-0.7Li samples exhibited a lower strength and elongation (416.5 MPa, 2.3%). The comparably lower mechanical performance

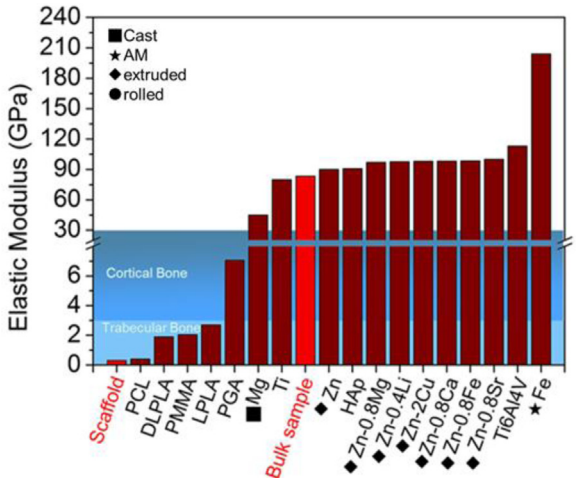

Fig. 15. Elastic modulus of various biomaterials: polymers [48], HAp [49], Ti and Ti6Al4V [50,51], Mg [52], Fe [53] and Zn-based metals [19].

is attributed to the formation quality and microstructure. Even under the optimized condition, tiny pores and cracks were found at the cross-section in Fig. 2 and the fracture surfaces as shown in Fig. 6. According to the literature, the ductility decreased with increasing the Li content in Zn-Li alloys. The casted Zn-0.8Li samples were also reported brittle with elongation as roughly 0.25% [17]. The ductility of Zn-Li alloys can be improved by refining and homogenizing the grain by plastic deformation. After the hot-warm rolling, the elongation of casted Zn-0.48Li increased from 0.5% to 46.5%, explained by the transformed hierarchical microstructure of the eutectic of Zn and β-$LiZn_4$ as well as primary β-$LiZn_4$ [14]. The elongation of Zn-0.8Li reached 75% after controlled hot rolling [18].

Compressive properties of porous samples were provided to show the capability of additive manufacture to customize the mechanical performance comparable to those of cancellous bone. Porous scaffolds are not only biologically conducive to cell proliferation, nutrient diffusion and bone integration, but also beneficial to mimic the mechanical performance of bone [24–27]. TPMS is defined as a 3D surface with a mean curvature of zero and periodic structures in three coordinate directions and is implicitly expressed using mathematical equations. TPMS-gyroid porous scaffolds possessed various excellent properties, such as interconnected open-pores, continuous and smooth transition and parameterized controlling of porosity [27]. Relatively high porosity of 80% was used to investigate the effect of pores on the mechanical and biological performance of Zn-0.7Li porous samples.

The compressive strength and elastic modulus of porous samples reduce to 18.2 MPa and 298.0 MPa. As shown in Fig. 15, the elastic modulus of cortical bone and cancellous bone are roughly 3–30 and 0.1- 3 GPa, respectively [23]. The high elastic modulus of bulk metals causes stress shielding, defined by the effect that the stress and strain on bone are suppressed. Stimulated by the applied stress, bone cells can properly adjust the formation of osteoblast and osteoclast, and reconstruct bone tissues to adapt to stress loading and to complete bone reconstruction [47]. The ability to modulate the elastic modulus of Zn alloys through alloying design is limited. Nevertheless, it is time-consuming and costly to develop new alloys, especially for medical applications. The elastic modulus of polymers is close to that of bone, but the strength of polymers is too low for load-bearing bone implants. Zn-0.7Li porous samples in this work exhibited equivalent elastic modulus to that of cancellous bone. The mechanical properties of porous scaffolds can be further adjusted by using customized pores units to meet patient-specific needs.

Table 2
Comparison of geometry and corrosion behavior of different samples.

Index	Unit	Porous cylinder	Bulk cylinder	Bulk cuboid
Outline size	mm^3	$\varphi 5\times 6$	$\varphi 5\times 6$	$8 \times 8^{*}2$
Surface area in design	mm^2	175	133.5	192
Volume in design	mm^3	23.6	117.8	128
Specific area in design	mm^{-1}	7.4	1.13	1.5
Weight loss	%	2.60	/	0.56
Corrosion rate	μm/year	35	/	46

4.3. Biodegradation and biocompatibility

The full degradation term of bulk Zn alloys in animals is estimated to be roughly 20 months, and the corrosion rate of Zn-Li alloys has been considered too slow for bone implants [19]. In this work, the corrosion rate and the weight loss of Zn-0.7Li as-built bulk samples after 28-day immersion was 46.2 ± 8.1 μm/year and 0.56% respectively. The PDP curve of polished bulk samples indicated a passivation effect and a much slower corrosion rate, which have been reported for casted and rolled Zn-Li alloy bulk samples [11,12,17,18]. The addition of Li suppresses the corrosion by forming a passive layer of corrosion products at the surface of Zn-Li alloys. Li exhibits greater mobility and activity compared with Zn and preferentially corrodes in an aqueous environment. The effect of Li addition on corrosion rate was explained by the interaction between the preferential dissolution of Li ions and the passive layer of Li-rich corrosion products. The Li-rich corrosion layer majorly contains LiOH and Li_2CO_3 for Zn-Li alloys [12], in agreement with the enrichment of elements O and C observed in Fig. 12(c).

According to the Zn-Li binary phase diagram, the eutectic reaction occurs when the Li content is greater than 0.1 wt.%, and the eutectic point is approximately 0.44 wt.%. The increased corrosion rate of Zn-(0.1–0.4)Li alloy is contributed to the galvanic reaction between precipitation phases and the substrate, which causes the preferential dissolution of Li ions. With a small addition of Li, the passivation resulting from the corrosion products is not enough to counteract the preferential dissolution. The decreased corrosion rate of Zn-(0.5–1.4)Li alloys owes to the continuous corrosion products of Li, which forms a passive layer and blocks the corrosion between the substrate and the aqueous solution [17].

For casted bulk samples, the I_{corr} decreased significantly from 3.08 μA/cm^2 for pure Zn to 1.38 μA/cm^2 for Zn-0.8Li alloy [17]. For the bulk samples in this work, the I_{corr} was 28.5 ± 1.6 μA/cm^2 for the polished surface and increased to 101.0 ± 4.1 μA/cm^2 for the as-built surface. The attached powder particles at the as-built surface diminished the passivation effect, thus increasing the corrosion rate. It is difficult to accurately measure the real surface area of the as-built samples. Thus, the surface area of all the samples was calculated according to the design data. As shown in Table 2, the surface area and volume of a cylinder bulk in size of φ 5 × 6 mm^3 is 133.45 mm^2 and 117.75 mm^3; while they are for 175 mm^2 and 23.56 mm^3 respectively for the porous scaffold in the same outline size. Although the volume of porous samples decreased by 80%, the surface still increased by 31% for the comparison. The specific area (the surface area divided by the volume) of the porous samples was as high as 6.55 times that of the bulk cylinder. The interconnected pores with a big specific area have been regarded as beneficial to osteoconduction and osteointegration of bone implants [47].

According to the 28-day immersion test in Hank's solution, the weight loss of porous samples was 4.64 times of bulk samples, close to the ratio of a specific area as shown in Table 2. A bigger specific area increased the contact with corrosion medium, thus resulting in a higher weight loss. Generally speaking, it takes 3–6 months for the bone to heal itself and recover the loading capacity, and the specific recovery term varies in different people and fractures sites [7]. The full degradation periods of pure Zn or Zn-Li alloys bulks are estimated much longer than the required term of bone recovery [19]. The faster degradation of porous scaffolds is regarded beneficial to match the term of bone recovery. However, if the corrosion rate of porous scaffolds is evaluated according to Eq. (6), the calculated value appears smaller than that of bulk samples as shown in Table 2. The commonly used Eq. (6) doesn't consider the effect of pores on the specific area. The weight loss is more accurate to indicate the influence of corrosion on the structural integrity of porous scaffolds. Meanwhile, it should be mentioned that the corrosion rate was overestimated for the as-built LPBF samples by using the surface area in design instead of the real surface area. The surface roughness, as shown in Fig. 7, considerably increased the surface area of the as-built samples.

The increased accumulation of Zn^{2+} ions damages the cytocompatibility of biodegradable Zn alloys since bone cells have a limited tolerance value to Zn^{2+} ions [4,9]. Superior cell viability and bone integration of Zn-Li alloys had been reported by *in vitro* and *in vivo* tests compared with pure Zn and other Zn alloys [19]. Li^{+} ion is released preferentially in the Zn-Li alloy and has a positive influence on bone formation via the activation of the canonical Wnt pathway [20,54]. The larger specific surface area and the curvatures of porous scaffolds are regarded as the major reasons for the improved cell viability [47].

Compared with bulk samples, the porous scaffolds exhibited lower elastic modulus, faster corrosion rate and improved cytocompatibility, all of which better meet the clinical needs as biodegradable bone implants. Moreover, additive manufacturing can accomplish the various porous design, thus providing tremendous opportunities to tailor the properties [23–26]. Regarding porous scaffolds, the strength and elastic modulus decrease with increasing the structural porosity; the degradation period decreases with increasing the specific area; the cell viability changes with pore size and morphology. Nevertheless, the presented results lead to several points for further investigation. Firstly, the present *in vitro* test doesn't consider the effect of dynamic fluid flow or stress. Secondly, the effect of porous design with different pore units on mechanical and biodegradable performance needs to be clarified. Various porous scaffolds can achieve the same structural porosity but may exhibit different mechanical and biodegradable performances. Thirdly, uniform corrosion is critical to porous scaffolds especially at the early stage when the loading capacity is required. Both the temporal and spatial degradation behavior needs to be studied. At last, the degradation of porous scaffolds and the growth of bone tissue interact with each other. The effect of degradation on the structural integrity of porous scaffolds and bone formation needs to be further evaluated by using appropriate in-vivo models.

5. Conclusion

This paper presented for the first time a comprehensive study on additively manufactured Zn-0.7Li alloy. The effects of Li addition, porous structure and processing conditions on the formation

quality, microstructure, mechanical properties, biodegradation, and biocompatibility were investigated.

With the atomized Zn-0.7Li powder and the optimized processing conditions, the relative density of bulk samples reached 99.5%, and the fabricated porosity of porous scaffolds was 78.9%, much close to the designed value of 80%. The good formation quality ensured stable biodegradable performance and credible evaluation. The Li content reduced from 0.69% in powder to 0.67% in LPBF samples. Refined α-Zn and β-$LiZn_4$ were observed with uniform distribution. The tensile strength and elastic modulus of bulk samples were 416.5 MPa and 83.3 GPa, while the compressive strength and elastic modulus of porous samples were 18.2 and 298.0 MPa respectively.

Passivation effect resulting from corrosion products was observed at the polished surface, but not at the as-built surface. The corrosion current by the electrochemical test was 28.5, 101.0 and 111.2 μA/cm^2 for the polished, as-built bulk and porous samples respectively. The as-built bulk and porous samples exhibited the weight loss of 2.60% and 0.56%, and the corrosion rate as 35 and 46 μm/year respectively by 28-day immersion test. Better cell adhesion and viability were found on porous samples in contrast with bulk samples.

Credit authorship contribution statement

Yu Qin: Conceptualization, Formal analysis, Investigation, Writing an original draft. **Hongtao Yang:** Supervision of biocompatibility and electrochemical tests, review. **Aobo Liu:** Processing and microstructural tests. **Jiabao Da:** Structural design of porous scaffold. **Yufeng Zheng:** Writing - review & editing, Supervision. **Yun Tian:** Formal analysis, Supervision. **Shuang Li:** Data curation, Investigation. **Xiaogang Wang:** Investigation, Visualization. **Peng Wen:** Writing - review & editing, Supervision.

Declaration of Competing Interest

The authors declare that they have no known competing financial interests or personal relationships that could have appeared to influence the work reported in this paper.

Acknowledgments

This work was supported by the National Key R&D Program of China (grant number 2018YFE0104200) and the National Natural Science Foundation of China (grant nos. 52175274, 51875310, 51931001, 52111530042, and 82172065).

Supplementary materials

Supplementary material associated with this article can be found, in the online version, at doi:10.1016/j.actbio.2022.01.049.

References

[1] F. Witte, The history of biodegradable magnesium implants: a review, Acta Biomater. 6 (5) (2010) 1680–1692, doi:10.1016/j.actbio.2010.02.028.
[2] Y.F. Zheng, X.N. Gu, F. Witte, Biodegradable metals, Mater. Sci. Eng: R: Reports 77 (2014) 1–34, doi:10.1016/j.mser.2014.01.001.
[3] J. Zhang, Y. Jiang, Z. Shang, B. Zhao, M. Jiao, W. Liu, M. Cheng, B. Zhai, Y. Guo, B. Liu, X. Shi, B. Ma, Biodegradable metals for bone defect repair: a systematic review and meta-analysis based on animal studies, Bioactive Mater. 6 (11) (2021) 4027–4052, doi:10.1016/j.bioactmat.2021.03.035.
[4] Y. Liu, Y. Zheng, X.H. Chen, J.A. Yang, H. Pan, D. Chen, L. Wang, J. Zhang, D. Zhu, S. Wu, Fundamental theory of biodegradable metals—definition, criteria, and design, Adv. Funct. Mater. 29 (18) (2019) 1805402, doi:10.1002/adfm.201805402.
[5] H.-.S. Han, S. Loffredo, I. Jun, J. Edwards, Y.-.C. Kim, H.-.K. Seok, F. Witte, D. Mantovani, S. Glyn-Jones, Current status and outlook on the clinical translation of biodegradable metals, Mater. Today 23 (2019) 57–71, doi:10.1016/j.mattod.2018.05.018.
[6] Y. Yang, C. He, E. Dianyu, W. Yang, F. Qi, D. Xie, L. Shen, S. Peng, C. Shuai, Mg bone implant: features, developments and perspectives, Mater. Des. 185 (2020) 108259, doi:10.1016/j.matdes.2019.108259.
[7] J. Venezuela, M.S. Dargusch, The influence of alloying and fabrication techniques on the mechanical properties, biodegradability and biocompatibility of zinc: a comprehensive review, Acta Biomater. 87 (2019) 1–40, doi:10.1016/j.actbio.2019.01.035.
[8] D. Hernández-Escobar, S. Champagne, H. Yilmazer, B. Dikici, C.J. Boehlert, H. Hermawan, Current status and perspectives of zinc-based absorbable alloys for biomedical applications, Acta Biomater. 97 (2019) 1–22, doi:10.1016/j.actbio.2019.07.034.
[9] G. Li, H. Yang, Y. Zheng, X.-.H. Chen, J.-.A. Yang, D. Zhu, L. Ruan, K. Takashima, Challenges in the use of zinc and its alloys as biodegradable metals: perspective from biomechanical compatibility, Acta Biomater. 97 (2019) 23–45, doi:10.1016/j.actbio.2019.07.038.
[10] H. Li, X. Xie, Y. Zheng, Y. Cong, F. Zhou, K. Qiu, X. Wang, S. Chen, L. Huang, L. Tian, Development of biodegradable Zn-1X binary alloys with nutrient alloying elements Mg, Ca and Sr, Sci. Rep. 5 (1) (2015) 1–14, doi:10.1038/srep10719.
[11] S. Zhao, C.T. McNamara, P.K. Bowen, N. Verhun, J.P. Braykovich, J. Goldman, J.W. Drelich, Structural characteristics and *in vitro* biodegradation of a novel Zn-Li alloy prepared by induction melting and hot rolling, Metall. Mater. Trans. A 48 (3) (2017) 1204–1215, doi:10.1007/s11661-016-3901-0.
[12] Z. Li, Z.-.Z. Shi, Y. Yan, D. Zhang, K. Yang, H.-.F. Li, H. Zhang, L.-.N. Wang, Suppression mechanism of initial pitting corrosion of pure Zn by Li alloying, Corros. Sci. (2021) 109564, doi:10.1016/j.corsci.2021.109564.
[13] S. Zhu, C. Wu, G. Li, Y. Zheng, J.-.F. Nie, Microstructure, mechanical properties and creep behaviour of extruded Zn-xLi (x= 0.1, 0.3 and 0.4) alloys for biodegradable vascular stent applications, Mat. Sci. Eng. A 777 (2020) 139082, doi:10.1016/j.msea.2020.139082.
[14] Z. Li, Z.-.Z. Shi, H.-.J. Zhang, H.-.F. Li, Y. Feng, L.-.N. Wang, Hierarchical microstructure and two-stage corrosion behavior of a high-performance near-eutectic Zn-Li alloy, J. Mater. Sci. Technol. 80 (2021) 50–65, doi:10.1016/j.jmst.2020.10.076.
[15] Z. Li, Z.-.Z. Shi, Y. Hao, H.-.F. Li, X.-.F. Liu, A.A. Volinsky, H.-.J. Zhang, L.-.N. Wang, High-performance hot-warm rolled Zn-0.8Li alloy with nano-sized metastable precipitates and sub-micron grains for biodegradable stents, J. Mater. Sci. Technol. 35 (11) (2019) 2618–2624, doi:10.1016/j.jmst.2019.06.009.
[16] H. Yang, X. Qu, M. Wang, H. Cheng, B. Jia, J. Nie, K. Dai, Y. Zheng, Zn-0.4Li alloy shows great potential for the fixation and healing of bone fractures at load-bearing sites, Chem. Eng. J. 417 (2021) 129317, doi:10.1016/j.cej.2021.129317.
[17] Z. Li, Z.-.Z. Shi, Y. Hao, H.-.F. Li, H.-.J. Zhang, X.-.F. Liu, L.-.N. Wang, Insight into role and mechanism of Li on the key aspects of biodegradable ZnLi alloys: microstructure evolution, mechanical properties, corrosion behavior and cytotoxicity, Mater. Sci. Eng.: C 114 (2020) 111049, doi:10.1016/j.msec.2020.111049.
[18] Y. Zhang, Y. Yan, X. Xu, Y. Lu, L. Chen, D. Li, Y. Dai, Y. Kang, K. Yu, Investigation on the microstructure, mechanical properties, *in vitro* degradation behavior and biocompatibility of newly developed Zn-0.8% Li-(Mg, Ag) alloys for guided bone regeneration, Mater. Sci. Eng.: C 99 (2019) 1021–1034, doi:10.1016/j.msec.2019.01.120.
[19] H. Yang, B. Jia, Z. Zhang, X. Qu, G. Li, W. Lin, D. Zhu, K. Dai, Y. Zheng, Alloying design of biodegradable zinc as promising bone implants for load-bearing applications, Nat. Commun. 11 (1) (2020) 1–16, doi:10.1038/s41467-019-14153-7.
[20] P. Clément-Lacroix, M. Ai, F. Morvan, S. Roman-Roman, B. Vayssière, C. Belleville, K. Estrera, M.L. Warman, R. Baron, G. Rawadi, Lrp5-independent activation of Wnt signaling by lithium chloride increases bone formation and bone mass in mice, Proc. Natl. Acad. Sci. 102 (48) (2005) 17406–17411, doi:10.1073/pnas.0505259102.
[21] S. Bose, D. Ke, H. Sahasrabudhe, A. Bandyopadhyay, Additive manufacturing of biomaterials, Prog. Mater Sci. 93 (2018) 45–111, doi:10.1016/j.pmatsci.2017.08.003.
[22] S.L. Sing, J. An, W.Y. Yeong, F.E. Wiria, Laser and electron-beam powder-bed additive manufacturing of metallic implants: a review on processes, materials and designs, J. Orthop. Res. 34 (3) (2016) 369–385, doi:10.1002/jor.23075.
[23] X. Wang, S. Xu, S. Zhou, W. Xu, M. Leary, P. Choong, M. Qian, M. Brandt, Y.M. Xie, Topological design and additive manufacturing of porous metals for bone scaffolds and orthopaedic implants: a review, Biomaterials 83 (2016) 127–141, doi:10.1016/j.biomaterials.2016.01.012.
[24] A. Zadpoor, Additively manufactured porous metallic biomaterials, J. Mater. Chem. B 7 (2019) 4088–4117, doi:10.1039/C9TB00420C.
[25] A.A. Zadpoor, Design for Additive Bio-Manufacturing: from Patient-Specific Medical Devices to Rationally Designed Meta-Biomaterials, Int. J. Mol. Sci. 18 (8) (2017) 1607, doi:10.3390/ijms18081607.
[26] A. Zadpoor, Meta-biomaterials, Biomater. Sci. 8 (1) (2020) 18–38, doi:10.1039/C9BM01247H.
[27] F.S.L. Bobbert, K. Lietaert, A.A. Eftekhari, B. Pouran, S.M. Ahmadi, H. Weinans, A.A. Zadpoor, Additively manufactured metallic porous biomaterials based on minimal surfaces: a unique combination of topological, mechanical, and mass transport properties, Acta Biomater. 53 (2017) 572–584, doi:10.1016/j.actbio.2017.02.024.
[28] A.G. Demir, L. Monguzzi, B. Previtali, Selective laser melting of pure Zn with high density for biodegradable implant manufacturing, Additive Manuf. 15 (2017) 20–28, doi:10.1016/j.addma.2017.03.004.
[29] P. Wen, L. Jauer, M. Voshage, Y. Chen, R. Poprawe, J.H. Schleifenbaum, Densification behavior of pure Zn metal parts produced by selective laser melting for manufacturing biodegradable implants, J Mater Process Tech 258 (2018) 128–137, doi:10.1016/j.jmatprotec.2018.03.007.

[30] P. Wen, Y. Qin, Y. Chen, M. Voshage, L. Jauer, R. Poprawe, J.H. Schleifenbaum, Laser additive manufacturing of Zn porous scaffolds: shielding gas flow, surface quality and densification, J. Mater. Sci. Technol. 35 (2) (2019) 368–376, doi:10.1016/j.jmst.2018.09.065.
[31] P. Wen, M. Voshage, L. Jauer, Y. Chen, Y. Qin, R. Poprawe, J.H. Schleifenbaum, Laser additive manufacturing of Zn metal parts for biodegradable applications: processing, formation quality and mechanical properties, Mater. Des. 155 (2018) 36–45, doi:10.1016/j.matdes.2018.05.057.
[32] Y. Qin, P. Wen, M. Voshage, Y. Chen, P.G. Schückler, L. Jauer, D. Xia, H. Guo, Y. Zheng, J.H. Schleifenbaum, Additive manufacturing of biodegradable Zn-xWE43 porous scaffolds: formation quality, microstructure and mechanical properties, Mater. Des. 181 (2019) 107937, doi:10.1016/j.matdes.2019.107937.
[33] Y. Li, P. Pavanram, J. Zhou, K. Lietaert, P. Taheri, W. Li, H. San, M. Leeflang, J. Mol, H. Jahr, Additively manufactured biodegradable porous zinc, Acta Biomater. 101 (2020) 609–623, doi:10.1016/j.actbio.2019.10.034.
[34] Y. Li, P. Pavanram, J. Zhou, K. Lietaert, F. Bobbert, Y. Kubo, M. Leeflang, H. Jahr, A. Zadpoor, Additively manufactured functionally graded biodegradable porous zinc, Biomater. Sci. 8 (9) (2020) 2404–2419, doi:10.1016/j.actbio.2019.07.013.
[35] K. Lietaert, A.A. Zadpoor, M. Sonnaert, J. Schrooten, L. Weber, A. Mortensen, J. Vleugels, Mechanical properties and cytocompatibility of dense and porous Zn produced by laser powder bed fusion for biodegradable implant applications, Acta Biomater. 110 (2020) 289–302, doi:10.1016/j.actbio.2020.04.006.
[36] Y. Yang, F. Yuan, C. Gao, P. Feng, L. Xue, S. He, C. Shuai, A combined strategy to enhance the properties of Zn by laser rapid solidification and laser alloying, J. Mech. Behav. Biomed. Mater. 82 (2018) 51–60, doi:10.1016/j.jmbbm.2018.03.018.
[37] C. Shuai, Y. Cheng, Y. Yang, S. Peng, W. Yang, F. Qi, Laser additive manufacturing of Zn-2Al part for bone repair: formability, microstructure and properties, J. Alloy Compd. 798 (2019) 606–615, doi:10.1016/j.jallcom.2019.05.278.
[38] C. Shuai, L. Xue, C. Gao, Y. Yang, S. Peng, Y. Zhang, Selective laser melting of Zn–Ag alloys for bone repair: microstructure, mechanical properties and degradation behaviour, Virtual Phys. Prototyp. 13 (3) (2018) 146–154, doi:10.1080/17452759.2018.1458991.
[39] Y. Yang, Y. Cheng, S. Peng, L. Xu, C. He, F. Qi, M. Zhao, C. Shuai, Microstructure evolution and texture tailoring of reduced graphene oxide reinforced Zn scaffold, Bioactive Mater. 6 (5) (2021) 1230–1241, doi:10.1016/j.bioactmat.2020.10.017.
[40] Y. Qin, P. Wen, H. Guo, D. Xia, Y. Zheng, L. Jauer, R. Poprawe, M. Voshage, J.H. Schleifenbaum, Additive manufacturing of biodegradable metals: current research status and future perspectives, Acta Biomater. 98 (2019) 3–22, doi:10.1016/j.actbio.2019.04.046.
[41] T. DebRoy, H.L. Wei, J.S. Zuback, T. Mukherjee, J.W. Elmer, J.O. Milewski, A.M. Beese, A. Wilson-Heid, A. De, W. Zhang, Additive manufacturing of metallic components – Process, structure and properties, Prog. Mater Sci. 92 (2018) 112–224, doi:10.1016/j.pmatsci.2017.10.001.
[42] K.A. Yakimovich, A.G. Mozgovoi, Experimental investigation of the density and surface tension of molten lithium at temperatures up to 1300K, High Temp. 38 (2000) 657–659, doi:10.1007/BF02755816.
[43] N.T. Ban, C.M. Randall, D.J. Montgomery, Effect of isotopic mass on viscosity of molten lithium, Phys. Rev. 128 (1) (1962) 6–11, doi:10.1103/PhysRev.128.6.
[44] R. Xiao, X. Zhang, Problems and issues in laser beam welding of aluminum–lithium alloys, J. Manuf. Process. 16 (2) (2014) 166–175, doi:10.1016/j.jmapro.2013.10.005.
[45] D. Liu, B. Yürekli, T. Ullsperger, G. Matthäus, L. Schade, S. Nolte, M. Rettenmayr, Microstructural aspects of additive manufacturing of AlLi alloys with high Li content, Mater. Des. 198 (2021) 109323, doi:10.1016/j.matdes.2020.109323.
[46] A. Klassen, V. Forster, V. Juechter, C. Korner, A multi-component evaporation model for beam melting processes, Model. Simul. Mater. Sci. Eng. 25 (2017) 025003, doi:10.1088/1361-651X/aa5289.
[47] A.A. Zadpoor, Bone tissue regeneration: the role of scaffold geometry, Biomater. Sci. 3 (2) (2015) 231–245, doi:10.1039/C4BM00291A.
[48] Y. Onuma, P.W. Serruys, Bioresorbable scaffolds: from Basic Concept to Clinical Applications, CRC Press, 2017.
[49] C. Gautam, S. Kumar, V.K. Mishra, S. Biradar, Synthesis, structural and 3-D architecture of lanthanum oxide added hydroxyapatite composites for bone implant applications: enhanced microstructural and mechanical properties, Ceram. Int. 43 (16) (2017) 14114–14121, doi:10.1016/j.ceramint.2017.07.150.
[50] D. Banerjee, J. Williams, Perspectives on titanium science and technology, Acta Mater. 61 (3) (2013) 844–879, doi:10.1016/j.actamat.2012.10.043.
[51] M. Geetha, A.K. Singh, R. Asokamani, A.K. Gogia, Ti based biomaterials, the ultimate choice for orthopaedic implants–a review, Prog. Mater Sci. 54 (3) (2009) 397–425, doi:10.1016/j.pmatsci.2008.06.004.
[52] T. Sumitomo, C. Cáceres, M. Veidt, The elastic modulus of cast Mg–Al–Zn alloys, J. Light Met. 2 (1) (2002) 49–56, doi:10.1016/S1471-5317(02)00013-5.
[53] B. Song, S. Dong, Q. Liu, H. Liao, C. Coddet, Vacuum heat treatment of iron parts produced by selective laser melting: microstructure, residual stress and tensile behavior, Mater. Des. 54 (2014) 727–733, doi:10.1016/j.matdes.2013.08.085.
[54] A. Zamani, G.R. Omrani, M.M. Nasab, Lithium's effect on bone mineral density, Bone 44 (2) (2009) 331–334, doi:10.1016/j.bone.2008.10.001.